Supporting Information

Material and Methods

Constructs

The cDNA encoding rabbit HCN4 (GenBank: NM_001082707) and carrying an internal deletion (from residues 783 to 1064) was previously cloned into a modified pEG BacMam vector (1) (hereafter pEGA) for large-scale protein purification from mammalian cells. The internal deletion eliminates a poorly conserved region in the C-terminal portion of the HCN channel protein, but preserves all biophysical properties of HCN4 (slower kinetics, hyperpolarized $V_{1/2}$, large response to cAMP) as reported (2, 3). The final plasmid was termed pEGA: HCN4 (2). For whole-cell patch clamp analysis, the rabbit HCN4 cDNA was previously cloned into the pCI vector as reported in (4). C479S, Y507A, F510A, I511A, Y507A-F510A, Y507A-I511A, F510A-I511A mutations were generated by site-directed mutagenesis (QuikChange site-directed mutagenesis kit; Agilent Technologies) and confirmed by sequencing.

Protein expression and purification

Freestyle HEK293-F cell cultures (Thermo Fisher) were transiently transfected with pEGA: HCN4 (1 µg per ml) according to the procedure detailed in (2, 5). Membrane isolation and HCN4 purification were pursed according to the protocol details in (2, 5). The decahistidine-eGFP tag at the N terminus of HCN4 protein was not removed because 1) it is necessary for the Ivabradine binding assay (see chapter "fluorescence Size Exclusion Chromatography-based Thermostability - fSEC-TS) and 2) this does not affect high-resolution 3D structure determination by cryo-EM (Saponaro et al., 2021). Purified protein, hereafter GFP-HCN4, is kept in solution in a buffer containing 200 mM NaCl, 20 mM HEPES pH 7.0 and detergent (LMNG-CHS) at the concentration of 0.002% (w/v). For both cryo-EM structure determination and ligand binding assay, Ivabradine (Sigma) was dissolved in MilliQ water at 10 mM (stock concentration) and added to the protein sample at 0.5 mM final concentration.

Fluorescence Size Exclusion Chromatography-based Thermostability (fSEC-TS)

fSEC-TS assay was performed following the protocol detailed in (2, 6). Briefly, aliquots of purified protein (5µg) were heated for 10 min over the following range of temperatures: 20, 30, 40, 50, 55, 60, 65, 70, 80°C. the samples were centrifuged (30 min, at 18000 xg) to remove precipitated protein and the supernatant was loaded on a Superose 6 increase 10/300 GL SEC column (GE Healthcare Life Sciences) pre-equilibrated with buffer containing 200 mM NaCl, 20 mM HEPES pH 7.0 and detergent (LMNG-CHS) at the concentration of 0.002% (w/v) and connected to a Prominence UFLC system (Shimadzu) possessing a RF-10AXL fluorescence detector (Shimadzu) to monitor the emission signal (509 nm) of the excited GFP fused at the N terminus of HCN4. Thermal denaturation curves were obtained by measuring the height of the fluorescent SEC (fSEC) peak measured from samples at each of the different temperatures above reported. The height of the fSEC peak for sample incubated at 20°C was used as control for normalization. The thermal denaturation curves were fitted with a sigmoidal dose-response equation: $Y= A1+(A2-A1)/(1+10\wedge((LOGx0-x)*p))$

where Y is the fluorescence emission in arbitrary units, A1 the minimal fluorescence (from the sample heated at 80°C), A2 the maximal fluorescence (from the sample heated at 20°C), LOGx0 the melting temperature (Tm), x a given temperature, and p is the Hill slope. Mean Tm values were obtained by fitting individual curves from each experiment to the Boltzmann equation and then averaging all the obtained values. Data were analysed Origin (OriginLab) software and are presented as mean ± SEM. Statistical analysis was performed with the student's t-test for unpaired data.

Cryo-EM sample preparation and image acquisition

A 3 μL droplet of freshly purified GFP-HCN4, at final concentration of 0.5 mg/ml, and supplemented with 0.5 mM Ivabradine, was applied onto a UltrAu R0.6/1.0 300-mesh gold holey grid (Quantifoil), previously glow discharged for 30 s at 30mA using a GloQube system (Quorum Technologies). Following an incubation of 90 s at 4°C and 100% relative humidity, the grid was blotted and plunge-frozen in liquid ethane using a Vitrobot Mk IV (Thermo Fischer Scientific). Grids were imaged on a Titan Krios electron microscope (FEI) operating at 300kV acceleration voltage (7). Data collection was achieved with EPU automated data collection software (Thermo Fischer Scientific). 31670 exposure movies were collected at nominal magnification of 105,000 ×, corresponding to a pixel size of 0.84 Å/pixel at the specimen level, with an applied defocus range of −1.0 to −2.2 μm, in 0.2 μm steps. Movies were acquired using K3 direct electron detector (Gatan), mounted on a Gatan Bioquantum LS/967 energy filter, and operating in electron counting mode (16.9 e-/pixel/s) with a total exposure time of 1.7 s and a total accumulated dose of 40.7 e-/A^2, equally distributed over 40 movie fractions (1.02 e-/A^2 per fraction).

Single-particle analysis

Initial steps of data processing were performed using RELION-3.1 (8). Images were subjected to motion-correction and dose-weighting using MotionCor2 (version 1.2.1) (9). Estimation of the contrast transfer function (CTF) was performed on aligned, not weighted sum images using CTFFIND4 (version 4.1.10) (10). Template picking runs were done in RELION-3.1 using templates, low-pass filtered to 20 Å, which corresponded to top, bottom and side views and resulted in 1808144 picked particles. An additional picking run was performed on WARP (2511428 picked particles). Merged particles were subjected to several rounds of 2D classification to remove junk particles. An initial 3D auto-refinement was performed using as reference the HCN4 map EMDB: EMD-12512 (2), low-pass filtered at 30 Å. Subsequent rounds of 3D classification were then performed. A final dataset of 444873 particles were selected, extracted with recentred coordinates and an unbinned box size of 400 pixels and moved into CryoSPARCv3.3.1. Duplicate particles were removed and ab-initio reconstruction without symmetry constraints produced a volume with apparent C4 symmetry. This map was used for a 3D classification (heterogeneous refinement with four classes) without imposing symmetry. 107523 particles from to the best class were subjected to a non-uniform refinement, again without imposing symmetry, and a 3.6 Å mean reconstruction was obtained. From this map an initial 3D model structure of HCN4 was generated (for details see chapter "Model building, refinement, and validation").

Model building, refinement, and validation

HCN4 – IVA 3D model was based on the HCN4 cryo-EM structure (PDB: 7NP3) (2). The initial model was rigid body fitted into the cryo-EM reconstructions using UCSF CHIMERA (11) and the resulting

aligned model were subjected to real-space refinement using PHENIX (12) before sequence adjustment and manual model building with COOT (13). Subsequent HCN4 – IVA model was rigid body fitted with UCSF CHIMERA and real-space refinement with PHENIX using the previous HCN4 apo/AM coordinates as template (PDB: 7NMN) (2). A polyalanine truncation and a subsequent rigid body refinement with non-crystallographic symmetry (NCS) restrains was carried out with each model to properly assess NCS using PHENIX. A model with the library for the geometry restrains for Ivabradine was generated with Grade Web Server (Smart, O.S., Sharff A., Holstein, J., Womack, T.O., Flensburg, C., Keller, P., Paciorek, W., Vonrhein, C. and Bricogne G. (2021) Grade2 version 1.5.0. Cambridge, United Kingdom: Global Phasing Ltd.). The full atomic models of HCN4 – IVA was subjected to multiple rounds of real-space refinement in PHENIX including global minimization and refinement of atomic displacement parameters, and applying secondary structures, Ramachandran and NCS restrains (14).

MD simulations and trajectory analysis

Using CHARMM-GUI, the simulation system was generated by inserting the pore domain (L412-S523) of the HCN4 – IVA 3D model structure solved by cryo-EM (see chapter "Model building, refinement, and validation") in a pre-equilibrated 1-palmitoyl-2-oleoyl-sn-glycero-3-phosphocholine (POPC) bilayer consisting of 130 molecules. The combined channel-membrane system was solvated with 11370 H_2O molecules (15–17). Systems were prepared for both protonation states of ivabradine (with the tertiary amine protonated for IVA^+/ deprotonated for neutral IVA). To neutralize the system net charge and yield a final ion concentration of 900 mM KCl, 191 potassium cations/184 chloride anions (183 Cl^- for simulations with neutral IVA) were included by random replacement of H_2O molecules.

Simulations were conducted using GROMACS with the Amber99sb*-ILDN force field for the protein together with the GAFF2 parameters for IVA^+/neutral IVA (18–23). GAFF2 parameters were generated using ACPYPE v. 2022.1.3 in combination with antechamber 19.0 using AM1/BCC charges (24–27). Furthermore, the TIP3P model and Berger-derived lipid parameters used for H_2O and POPC respectively, together with TIP3P-optimized Cheatham-Joung ion parameters for K^+ and Cl^- (28–31). For van-der-Waals interactions, a cutoff for distances above 1 nm was selected, for Coulomb interactions, the particle-mesh Ewald method was applied with a real space cut-off of 1 nm. Pressure and temperature were held constant at 1 bar and 310 K using the Berendsen (for equilibration)/Parrinello-Rahman barostat (for production simulations) and the V-rescale thermostat respectively (32–34). Simulations were conducted with an integration time step of 2 fs, with all hydrogen-containing bonds constrained using the LINCS algorithm (35).

Energy minimization (EM), equilibration and production simulations followed a procedure employed in (2): Prior to production simulations, EM was conducted over 2000 steps with a step-width of 0.1 Å and the steepest-descent integrator, followed by NVT equilibration over 100 ps with restrained protein backbone and sidechains (Fc = 1000 kJ mol^{-1} nm^{-2}). Equilibration proceeded with simulations over 20 ns in the NPT ensemble; restraints on backbone and sidechains were gradually lifted in the following successive NPT simulations. To retain the HCN4 pore in its open-conductive state, harmonic distance restraints were applied to residues A415, I511, T515 and G519 using PLUMED (36). Simulations were generally conducted at -500 mV and -700 mV, with simulation times between 500 ns and 1 µs. Higher, non-physiological voltages are commonly employed in MD simulations of ion channels; in the case of

HCN4, these voltages offset the low unitary conductance and allow for sufficient sampling with reasonable computing time (37, 38).

All trajectories were analysed using Biotite versions 0.35-0.37 and GROMACS (19, 39). Additional Python packages used include NumPy and Pandas for data analysis, Matplotlib and Seaborn for data visualization and Snakemake for workflow management (40–42). Channel cavities were surveyed with HOLE version 2.3.1 (43).

Electrophysiology

Patch clamp recordings were carried out on HEK293T cells or HEK293F cells. HEK293T cells were cultured in DMEM high glucose medium (Euroclone) supplemented with 10% FBS (Euroclone) and 1% Penicillin-Streptomycin (Sigma). HEK293F were grown in Freestyle medium (Thermo Fisher) supplemented with 10% FBS (Euroclone) and 1% Penicillin-Streptomycin (Sigma). Both cell types were grown at 37°C with 5% CO_2. When 70% confluent, cells were transfected with 1 µg of rabbit pCI: HCN4 (wt or mutant), 0.3 µg of GFP-containing vector (pmax-GFP), and Turbofect transfection reagent (Thermo Fisher). HCN4 currents were recorded at room temperature, in whole cell configuration, using an ePatch (Elements srl) or a Dagan 3900A amplifier (Dagan Corporation). Signals acquired with the Dagan 3900A were digitized using a Digidata 1550B (Moelcular Devices). Measurements were performed as detailed in Porro et al., 2019, 2020; Saponaro et al., 2018. Patch pipettes were filled with a solution containing 10 mM NaCl, 130 mM KCl, 1 mM egtazic acid (EGTA), 0.5 mM $MgCl_2$, 2 mM ATP (magnesium salt), and 5 mM HEPES–KOH buffer (pH 7.2), while the extracellular bath solution contained 110 mM NaCl, 30 mM KCl, 1.8 mM $CaCl_2$, 0.5 mM $MgCl_2$, and 5 mM HEPES–KOH buffer (pH 7.4). Ivabradine (Sigma) was dissolved in MilliQ water at 10 mM (stock concentration) and added to the extracellular solution at 30 or 300 µM final concentration.

To obtain HCN4 channel activation curves, a series of voltage steps ranging from -30 mV to -150 mV (-15 mV increments, 4.5 s) were applied starting from a holding potential of -20 mV (1 s); tail currents were collected at -40 mV (4.5 s). Mean activation curves were obtained by fitting maximal tail current amplitude, plotted against the preconditioning voltage step, with the Boltzmann equation:

$$y = 1/[1+\exp((V-V_{1/2})/k)]$$

where V is voltage, y the fractional activation, $V_{1/2}$ the half-activation voltage, and k the inverse-slope factor in mV (k = -RT/zF). Mean activation curves were obtained by fitting individual curves from each cell to the Boltzmann equation and then averaging all the obtained values.

Ivabradine block was studied by superfusing the drug during repetitive application of activating (-140 mV; 0.6 s, 1 s or 1.5 s) and deactivating (+5 mV, 0.3 s or 0.7 s or 5.6s) voltage steps every 4 seconds, from a holding potential of -20 mV, until development of the full block. The duration of hyperpolarizing and depolarizing pulses was adjusted in each experiment to account for changes in current kinetics and allow HCN4 to reach full activation. For mutant F510A, to ensure complete deactivation of the channel and speed up deactivation kinetics, the duration of the deactivating step was increased to 5.6 s, the frequency of stimulation was set to 0.1 Hz and experiments were carried out at a controlled temperature of 34°C. Fractional current block was calculated as the ratio between the steady state current at the full block and the steady state current measured at -140 mV, just before the drug application. Kinetics of ivabradine block were calculated by fitting current vs time data with a single exponential function. Data

were analysed with Clampfit (Molecular devices) and Origin (OriginLab) softwares and are presented as mean ± SEM. Statistical analysis was performed with the student's t-test for unpaired data.

Supporting Figures

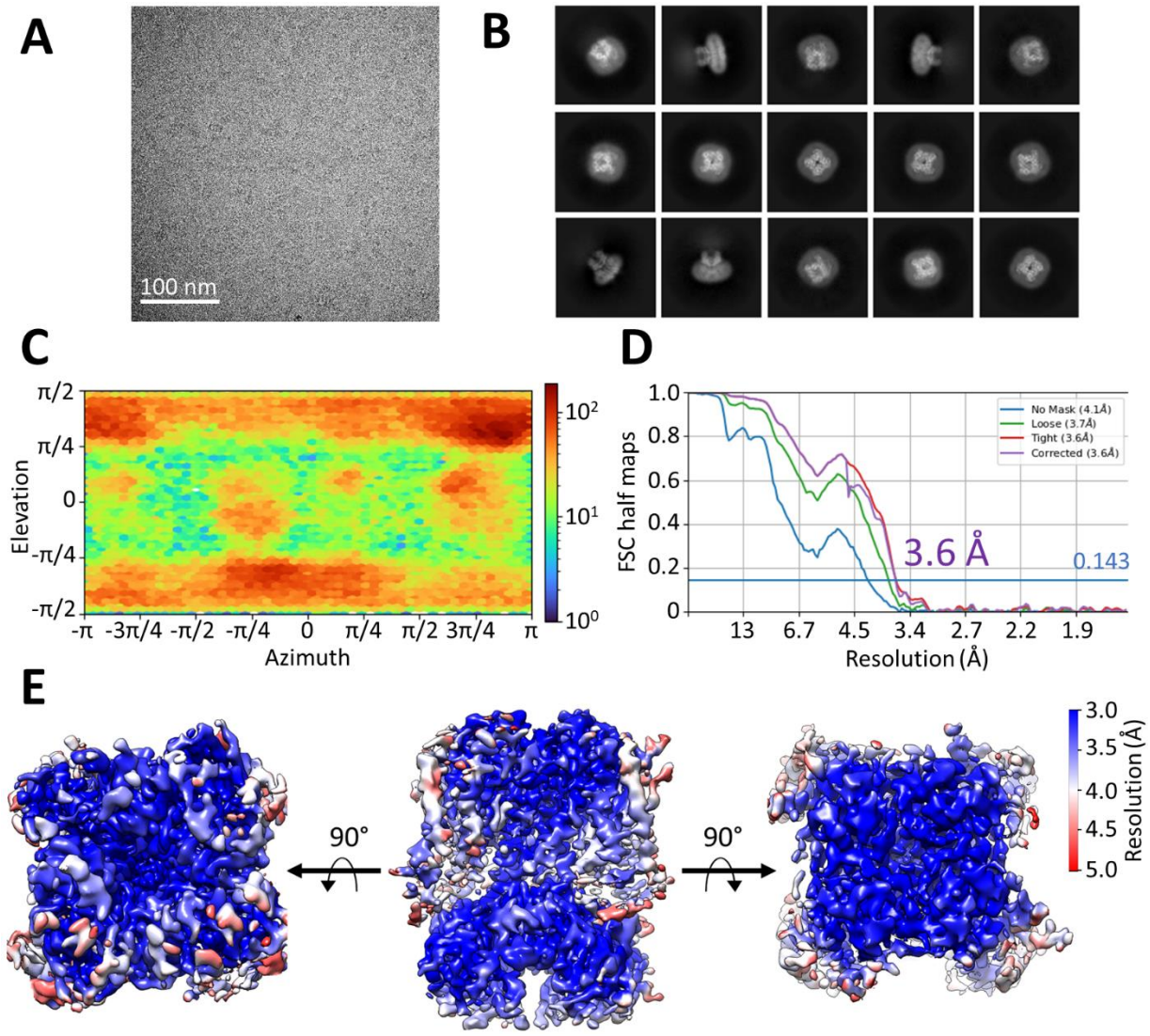

Figure S1: cryo-EM data analysis of HCN4 bound to Ivabradine.

A, Representative micrograph, and **B**, 2D classes with box size of 336 Å for HCN4 bound to Ivabradine. **C**-**F**, Three-dimensional reconstruction without imposing symmetry. **C**, Heat map of the Euler angle distribution of particle orientations from the three-dimensional reconstruction. **D**, Fourier shell correlation (FSC) curves between the two independently refined half-maps of final cryo-EM 3D reconstruction. **E**, Orthogonal views of the final cryo-EM 3D reconstruction colored by local resolution.

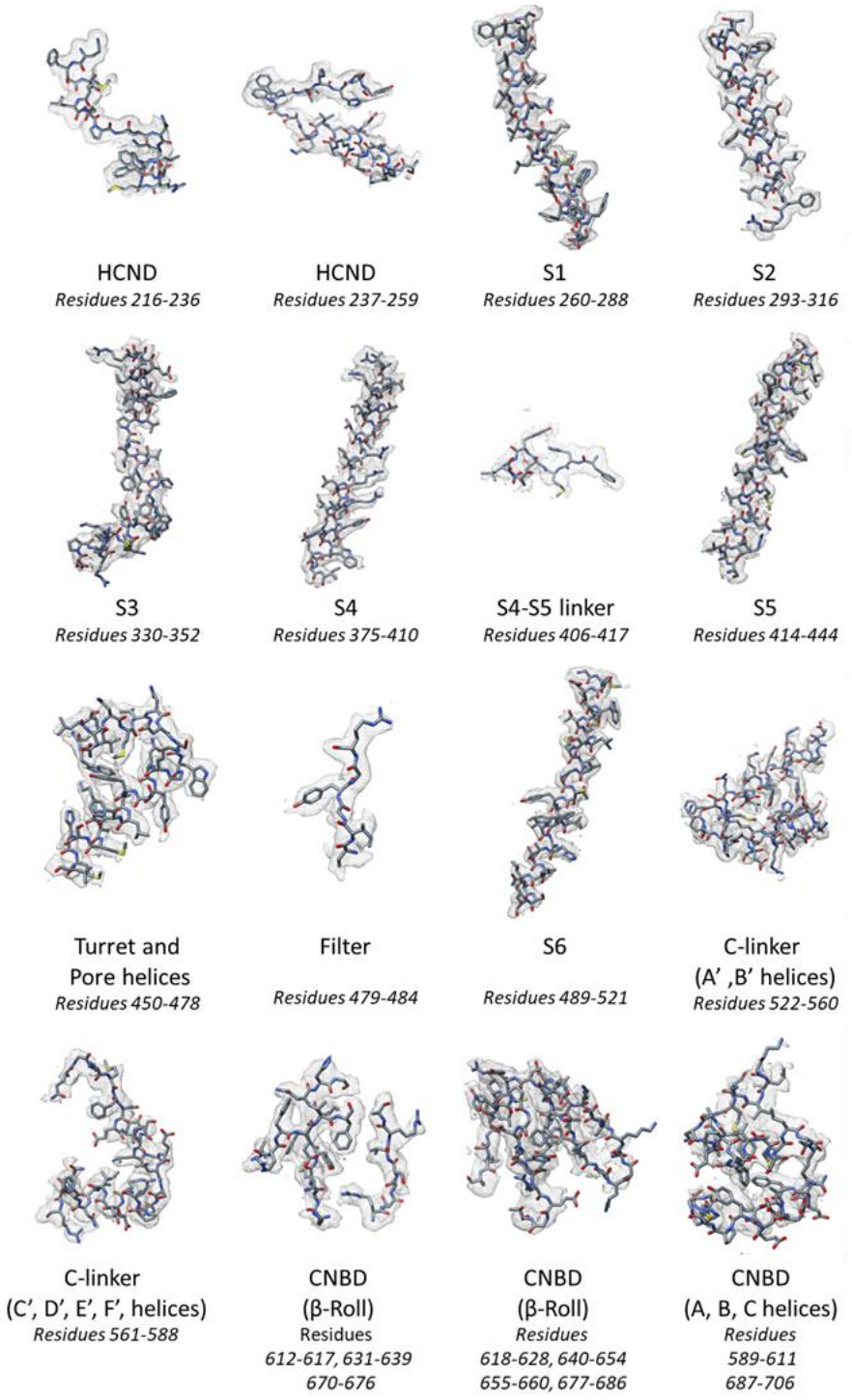

Figure S2: Cryo-EM density for HCN4 bound to Ivabradine.

Structural elements of HCN4, as indicated by the figure labels, with model (Chain A, dark gray stick) and superimposed density map (light gray mesh).

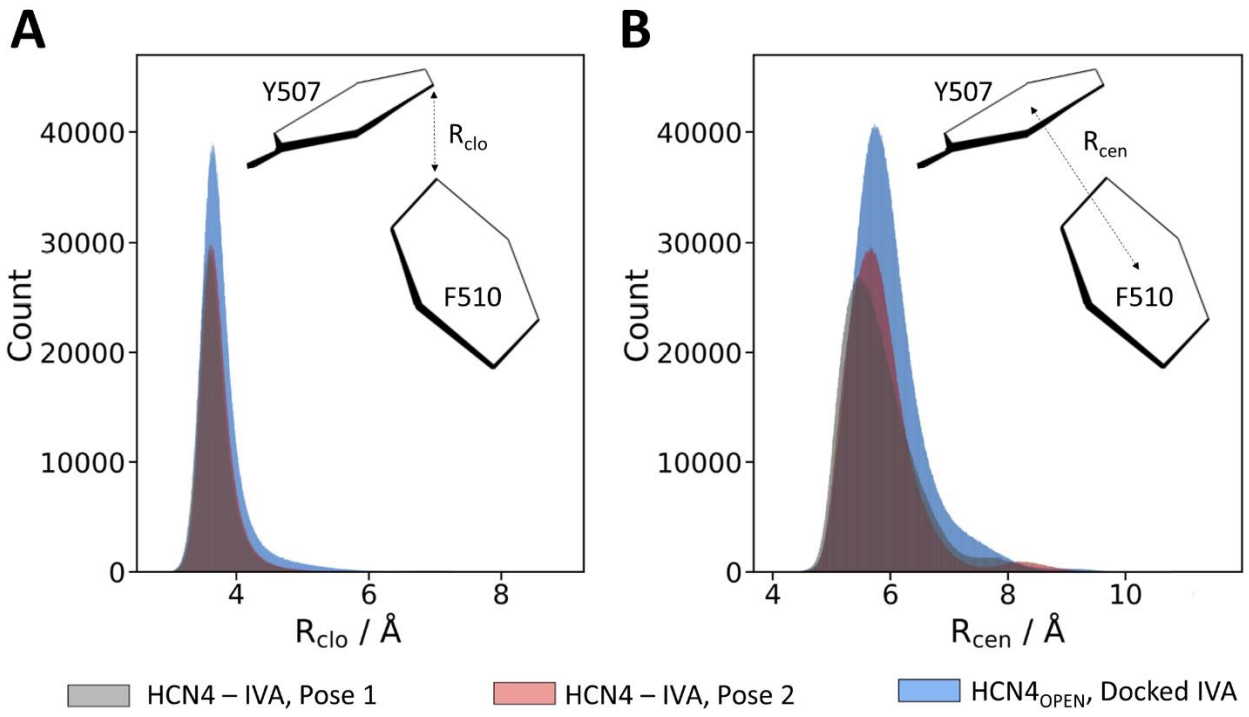

Figure S3: Distances between side chains of Y507 and F510 are compatible with π-stack. The minimum contact distances between respective carbons (R_{clo}) (**A**) and the inter-centroid distance R_{cen} (**B**) of the two aromatic rings were measured for all simulations run at -500 mV and aggregated with respect to starting structures**.** MD simulations of HCN4 open pore containing Ivabradine pose 1 and pose 2 are colored in gray and red, respectively, whereas MDs of HCN4 open pore containing Ivabradine docked as in Saponaro et al., 2021 is colored in blue. Insets of panel A and B depict the measured distances R_{clo} and R_{cen}, respectively. Maxima of both distance distributions are below 4.5 Å and 7.5 Å for R_{clo} and R_{cen}, respectively. These distance thresholds were adapted from the analysis of hydrophobic interaction between aromatic amino acids pairs of McGaughey et al., 1998.

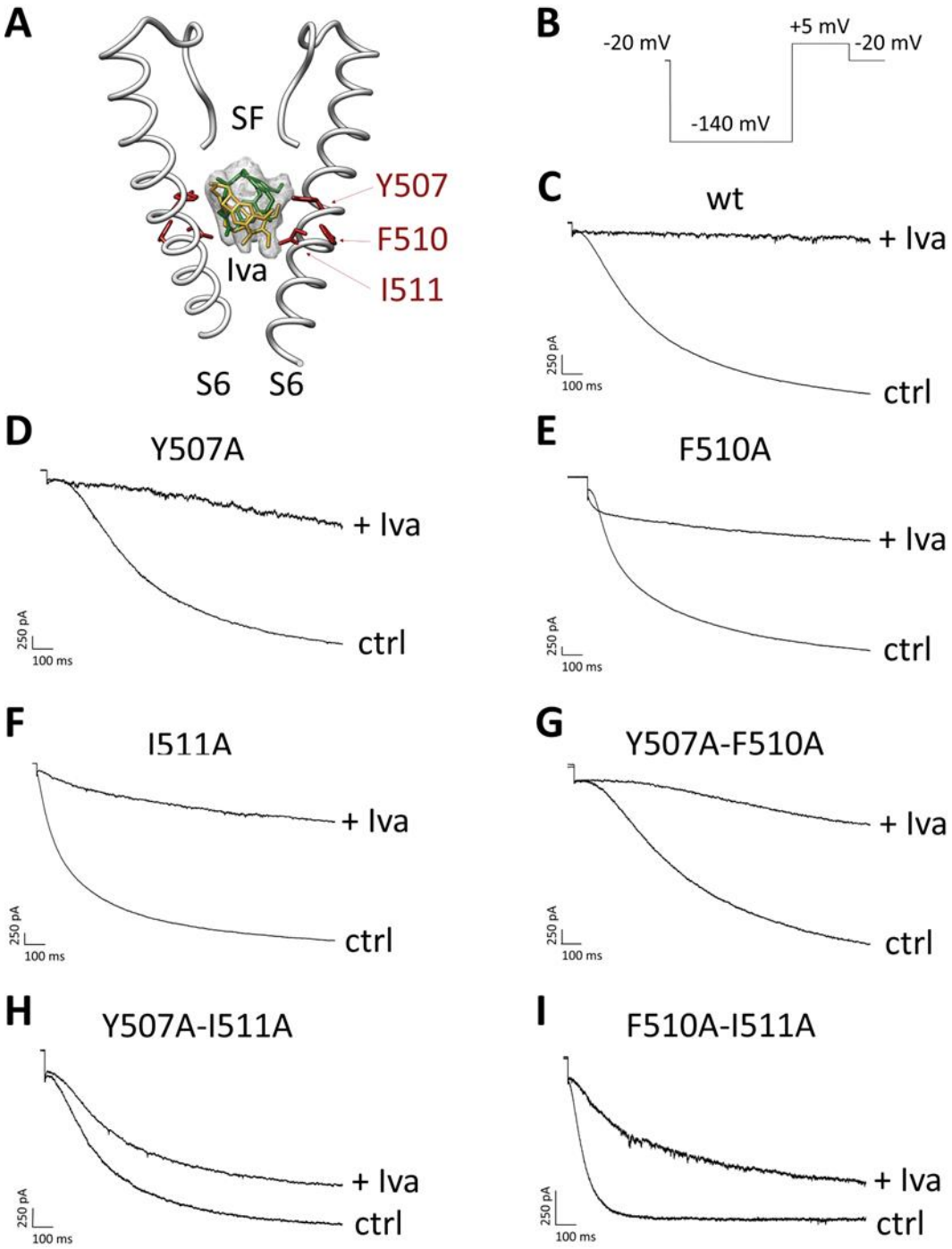

Figure S4: 300 µM Ivabradine block on HCN4 wt and mutants.

A, Cross-membrane view of HCN4 pore (S6) bound to Ivabradine (green/yellow sticks and gray density), (PDB: 8OFI). For clarity, only two opposite subunits of the tetramer are shown. Y507, F510, and I511 are shown as red sticks and labeled. **B**, Protocol used to study Ivabradine block: Drug was perfused

during repetitive application of activating (-140 mV; 0.6 s or 1.5 s) and deactivating (+5 mV, 0.3 s) voltage steps every 4 seconds, from a holding potential of -20 mV, until development of the full block. The duration of the hyperpolarizing pulse was adjusted in each experiment to account for changes in current kinetics and allow HCN4 to reach full activation. **C-I**, Representative current traces of HCN4 wt (**C**), Y507A (**D**), I511A (**E**), F510A (**F**), Y507A-F510A (**G**), Y507A-I511A (**H**), and F510A-I511A (**I**) in control (ctrl) and after superfusion with 300 µM Ivabradine (+ Iva) at steady-state block.

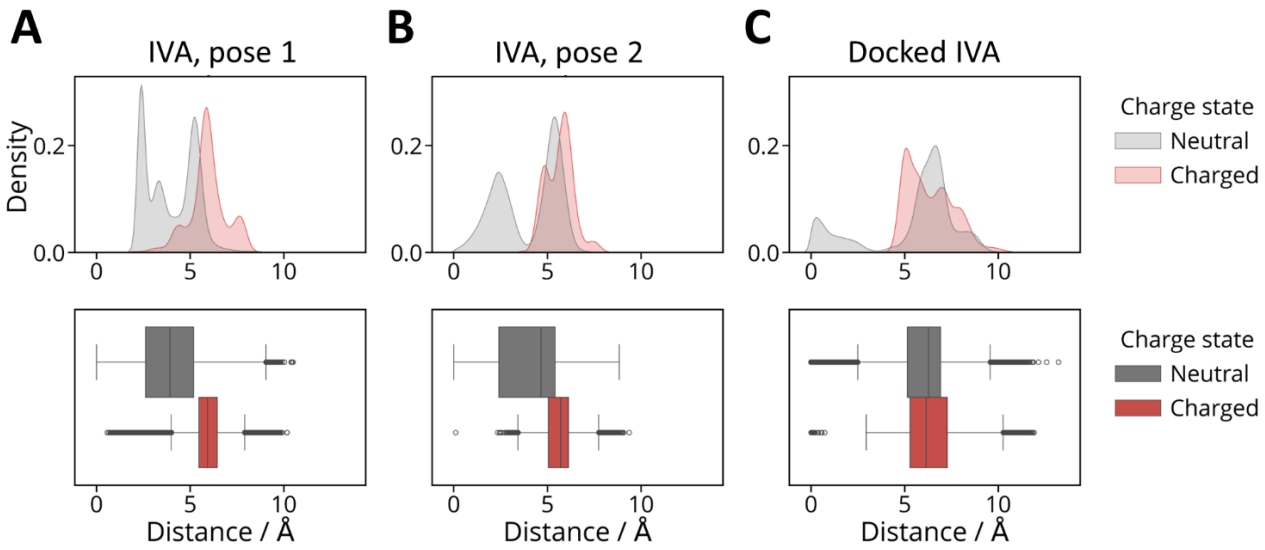

Figure S5: Distance distributions between N atom (tertiary amine) of Ivabradine, protonated and neutral, and K^+ along the main channel axis.

A-C, Distances between N (IVA) and K^+ derived from all simulations run at -500 mV are plotted as Kernel density estimate plot (top row) and boxplot (lower row). Simulations with neutral and charged IVA are colored in gray and red, respectively. **A**, MDs with pose 1; **B** MDs with pose 2; **C**, MDs with docked IVA that resembles the best-scoring docked pose within the open HCN4 channel previously published (Saponaro et al., 2021). In the boxplots, the box itself encompasses the Q1-Q3 interquartile range, while whiskers encompass the minimum/maximum datapoints within 1.5 x Q1-Q3. Outliers are depicted as gray circles.

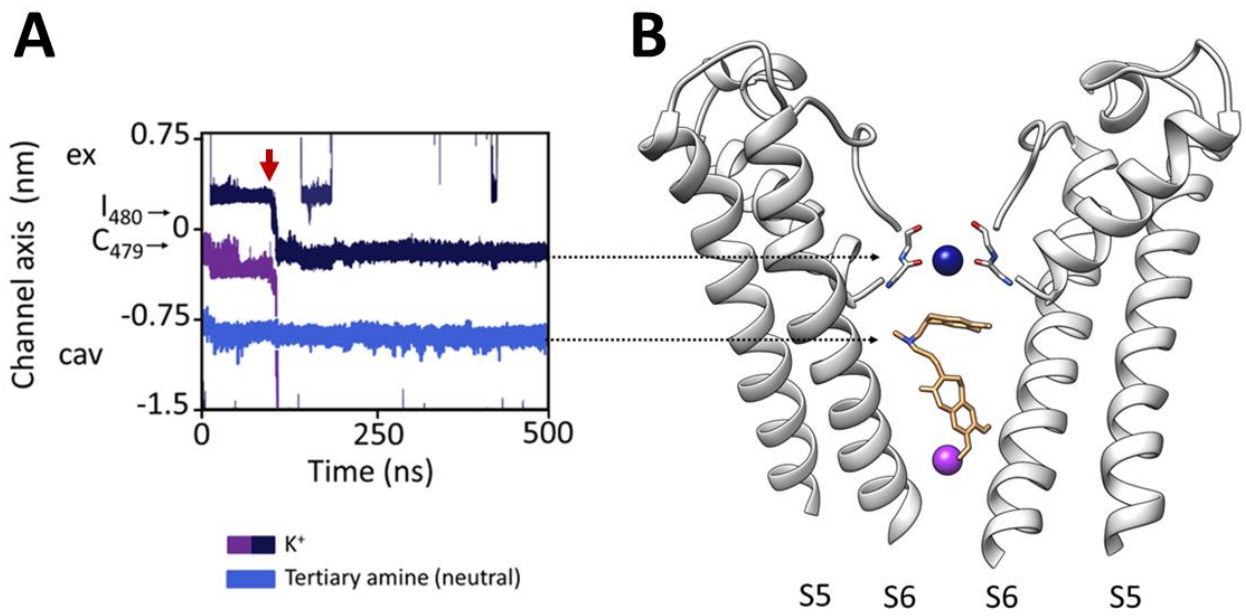

Figure S6: Full transition of the ion through the pore in the presence of neutral Ivabradine. A, 500 ns trajectories for the neutral tertiary amine of IVA-docked (light blue) and for K+ ions (purple and blue) in the HCN4 open pore. Positions of the carbonyl plane of C479 and I480 are indicated by black arrows. Ex (extracellular side of the pore); cav (intracellular pore cavity). **B**, representative snapshot of the MD simulation shown in the left panel (red arrow), cross-referenced with the latter by arrows. Entrance of a K^+ ion (blue) from extracellular side of SF moves the second ion (purple) from the lower SF to the intracellular pore cavity. Neutral Ivabradine (orange sticks) stably occupies the intracellular cavity even when a K^+ (purple) permeates the pore.

Table S1. Cryo-EM data collection, image processing and model refinement statistics.

Data collection and image processing	
Sample	HCN4 - IVA
Microscope	Titan Krios
Voltage (kV)	300
Camera	K3 (Gatan)
Magnification	105000
Total electron dose ($e^-/Å^2$)	40
Defocus range (μm)	-1.0 to -2.3
Pixel size (Å/pixel)	0.42 in superresolution (0.84 bin2)
Micrographs (no.)	31670
Symmetry imposed	C1
Initial particle images (no.)	444873
Final particle images (no.)	107523
Resolution (Å) (FSC threshold)	3.6
Sharpening B-factor ($Å^2$)	-109.1
EMDB code	EMD-16860
Model refinement	
Non hydrogen atoms	14765
Protein residues	1782
Ivabradine (IVR)	1
r.m.s. deviations	
Bond lengths (Å)	0.003
Bond angles (°)	0.686
Ramachandran plot	
Favored (%)	96.03
Allowed (%)	3.97
Disallowed (%)	0.00
Validation	
Molprobity score	1.93
Clashscore	14.10
Poor rotamers (%)	0.06
Map-model correlation	0.70
PDB code	8OFI

Table S2: Details of MD simulations.

Simulation	N replicas	Single simulations	t_{Sim} / ns	V / mV
IVA^{+}, pose 1	2	1 x 1 µs; 1 x 0.5 µs	1.5	-500
IVA^{+}, pose 2	2	1 x 1 µs; 1 x 0.5 µs	1.5	-500
Docked IVA^{+}	4	1 x 1 µs; 3 x 0.5 µs	2.5	-500
$IVA^{neutral}$, pose 1	2	2 x 1 µs	2	-500
$IVA^{neutral}$, pose 2	2	2 x 1 µs	2	-500
Docked $IVA^{neutral}$	4	1 x 1 µs; 3 x 0.5 µs	2.5	-500
Docked $IVA^{neutral}$	1	1 x 1 µs	1	-700
∑	17		13	

N replicas denotes the number of individual simulations run for a given initial structure, while V is the applied voltage in simulations. IVA^{+}/$IVA^{neutral}$ denote the protonation state of Ivabradine in the corresponding simulation, with the tertiary amine either protonated or deprotonated, respectively.

SI references

1. A. Goehring, *et al.*, Screening and large-scale expression of membrane proteins in mammalian cells for structural studies. *Nat Protoc* **9**, 2574–2585 (2014).

2. A. Saponaro, *et al.*, Gating movements and ion permeation in HCN4 pacemaker channels. *Mol Cell* **81**, 2929-2943.e6 (2021).

3. A. Saponaro, F. Vallese, A. Porro, O. B. Clarke, Validation of the binding stoichiometry between HCN channels and their neuronal regulator TRIP8b by single molecule measurements. *Front Physiol* **13**, 998176 (2022).

4. A. Saponaro, *et al.*, A synthetic peptide that prevents cAMP regulation in mammalian hyperpolarization-activated cyclic nucleotide-gated (HCN) channels. *Elife* **7** (2018).

5. A. Saponaro, A. S. Sharifzadeh, A. Moroni, Detection of ligand binding to purified HCN channels using fluorescence-based size exclusion chromatography. *Methods Enzymol* **652**, 105–123 (2021).

6. A. Saponaro, A. S. Sharifzadeh, A. Moroni, Detection of ligand binding to purified HCN channels using fluorescence-based size exclusion chromatography. *Methods Enzymol* **652**, 105–123 (2021).

7. E. Kandiah, *et al.*, CM01: a facility for cryo-electron microscopy at the European Synchrotron. *Acta Crystallogr D Struct Biol* **75**, 528–535 (2019).

8. J. Zivanov, *et al.*, New tools for automated high-resolution cryo-EM structure determination in RELION-3. *Elife* **7** (2018).

9. S. Q. Zheng, *et al.*, MotionCor2: anisotropic correction of beam-induced motion for improved cryo-electron microscopy. *Nat Methods* **14**, 331–332 (2017).

10. A. Rohou, N. Grigorieff, CTFFIND4: Fast and accurate defocus estimation from electron micrographs. *J Struct Biol* **192**, 216–221 (2015).

11. E. F. Pettersen, *et al.*, UCSF Chimera--a visualization system for exploratory research and analysis. *J Comput Chem* **25**, 1605–1612 (2004).

12. P. D. Adams, *et al.*, PHENIX: a comprehensive Python-based system for macromolecular structure solution. *Acta Crystallogr D Biol Crystallogr* **66**, 213–221 (2010).

13. P. Emsley, B. Lohkamp, W. G. Scott, K. Cowtan, Features and development of Coot. *Acta Crystallogr D Biol Crystallogr* **66**, 486–501 (2010).

14. P. V Afonine, *et al.*, Real-space refinement in PHENIX for cryo-EM and crystallography. *Acta Crystallogr D Struct Biol* **74**, 531–544 (2018).

15. S. Jo, T. Kim, V. G. Iyer, W. Im, CHARMM-GUI: A web-based graphical user interface for CHARMM. *J Comput Chem* **29**, 1859–1865 (2008).

16. J. Lee, *et al.*, CHARMM-GUI supports the Amber force fields. *J Chem Phys* **153**, 35103 (2020).

17. E. L. Wu, *et al.*, CHARMM-GUI Membrane Builder toward realistic biological membrane simulations. *J Comput Chem* **35**, 1997–2004 (2014).

18. M. J. Abraham, *et al.*, Gromacs: High performance molecular simulations through multi-level parallelism from laptops to supercomputers. *SoftwareX* **1–2**, 19–25 (2015).

19. H. J. C. Berendsen, D. van der Spoel, R. van Drunen, GROMACS: A message-passing parallel molecular dynamics implementation. *Comput Phys Commun* **91**, 43–56 (1995).

20. R. B. Best, G. Hummer, Optimized molecular dynamics force fields applied to the helix-coil transition of polypeptides. *J Phys Chem B* **113**, 9004–9015 (2009).

21. K. Lindorff-Larsen, *et al.*, Improved side-chain torsion potentials for the Amber ff99SB protein force field. *Proteins* **78**, 1950–1958 (2010).

22. S. Páll, M. J. Abraham, C. Kutzner, B. Hess, E. Lindahl, Tackling Exascale Software Challenges in Molecular Dynamics Simulations with GROMACS in *Solving Software Challenges for Exascale*, S. Markidis, E. Laure, Eds. (Springer International Publishing, 2015), pp. 3–27.

23. J. Wang, R. M. Wolf, J. W. Caldwell, P. A. Kollman, D. A. Case, Development and testing of a general amber force field. *J Comput Chem* **25**, 1157–1174 (2004).

24. A. Jakalian, D. B. Jack, C. I. Bayly, Fast, efficient generation of high-quality atomic charges. AM1-BCC model: II. Parameterization and validation. *J Comput Chem* **23**, 1623–1641 (2002).

25. A. Jakalian, B. L. Bush, D. B. Jack, C. I. Bayly, Fast, efficient generation of high-quality atomic charges. AM1-BCC model: I. Method. *J Comput Chem* **21**, 132–146 (2000).

26. A. W. Sousa da Silva, W. F. Vranken, ACPYPE - AnteChamber PYthon Parser interfacE. *BMC Res Notes* **5**, 367 (2012).

27. J. Wang, W. Wang, P. A. Kollman, D. A. Case, Automatic atom type and bond type perception in molecular mechanical calculations. *J Mol Graph Model* **25**, 247–260 (2006).

28. O. Berger, O. Edholm, F. Jähnig, Molecular dynamics simulations of a fluid bilayer of dipalmitoylphosphatidylcholine at full hydration, constant pressure, and constant temperature. *Biophys J* **72**, 2002–2013 (1997).

29. A. Cordomi, G. Caltabiano, L. Pardo, Membrane Protein Simulations Using AMBER Force Field and Berger Lipid Parameters. *J Chem Theory Comput* **8**, 948–958 (2012).

30. W. L. Jorgensen, J. Chandrasekhar, J. D. Madura, R. W. Impey, M. L. Klein, Comparison of simple potential functions for simulating liquid water. *J Chem Phys* **79**, 926–935 (1983).

31. I. S. Joung, T. E. 3rd Cheatham, Determination of alkali and halide monovalent ion parameters for use in explicitly solvated biomolecular simulations. *J Phys Chem B* **112**, 9020–9041 (2008).

32. H. J. C. Berendsen, J. P. M. Postma, W. F. van Gunsteren, A. DiNola, J. R. Haak, Molecular dynamics with coupling to an external bath. *J Chem Phys* **81**, 3684–3690 (1984).

33. G. Bussi, D. Donadio, M. Parrinello, Canonical sampling through velocity rescaling. *J Chem Phys* **126**, 14101 (2007).

34. M. Parrinello, A. Rahman, Polymorphic transitions in single crystals: A new molecular dynamics method. *J Appl Phys* **52**, 7182–7190 (1981).

35. B. Hess, H. Bekker, H. J. C. Berendsen, J. G. E. M. Fraaije, LINCS: A linear constraint solver for molecular simulations. *J Comput Chem* **18**, 1463–1472 (1997).

36. G. A. Tribello, M. Bonomi, D. Branduardi, C. Camilloni, G. Bussi, PLUMED 2: New feathers for an old bird. *Comput Phys Commun* **185**, 604–613 (2014).

37. A. E. V Andersson, M. A. Kasimova, L. Delemotte, Exploring the Viral Channel Kcv(PBCV-1) Function via Computation. *J Membr Biol* **251**, 419–430 (2018).

38. M. A. Kasimova, *et al.*, Helix breaking transition in the S4 of HCN channel is critical for hyperpolarization-dependent gating. *Elife* **8** (2019).

39. P. Kunzmann, K. Hamacher, Biotite: a unifying open source computational biology framework in Python. *BMC Bioinformatics* **19**, 346 (2018).

40. C. R. Harris, *et al.*, Array programming with NumPy. *Nature* **585**, 357–362 (2020).

41. J. D. Hunter, Matplotlib: A 2D Graphics Environment. *Comput Sci Eng* **9**, 90–95 (2007).

42. F. Mölder, *et al.*, Sustainable data analysis with Snakemake. *F1000Res* **10**, 33 (2021).

43. O. S. Smart, J. G. Neduvelil, X. Wang, B. A. Wallace, M. S. Sansom, HOLE: a program for the analysis of the pore dimensions of ion channel structural models. *J Mol Graph* **14**, 354-360,376 (1996).

44. A. Porro, *et al.*, The HCN domain couples voltage gating and cAMP response in hyperpolarization-activated cyclic nucleotide-gated channels. *Elife* **8** (2019).

45. A. Porro, *et al.*, Rational design of a mutation to investigate the role of the brain protein TRIP8b in limiting the cAMP response of HCN channels in neurons. *J Gen Physiol* **152** (2020).